The Astrophysical Journal, 930:74 (16pp), 2022 May 1 https://doi.org/10.3847/1538-4357/ac4fcb

Study of the Mass-loss Rate from the Sun

Grzegorz Michalek[1], Nat Gopalswamy[2], and Seiji Yashiro[2,3]
[1] Astronomical Observatory of Jagiellonian University, Krakow, Poland; grzegorz.michalek@uj.edu.pl
[2] NASA Goddard Space Flight Center, Greenbelt, MD 20771, USA
[3] The Catholic University of America, Washington, DC 20064, USA
Received 2021 November 22; revised 2022 January 26; accepted 2022 January 26; published 2022 May 4

Abstract

We investigate the temporal evolution of the yearly total mass-loss rate (YTMLR) from the Sun through coronal mass ejections (CMEs) over solar cycles 23 and 24. The mass determination of CMEs can be subject to significant uncertainty. To minimize this problem, we have used extensive statistical analysis. For this purpose, we employed data included in the Coordinated Data Analysis Workshop (CDAW) catalog. We estimated the contributions to mass loss from the Sun from different subsamples of CMEs (selected on the basis of their masses, angular widths, and position angles). The temporal variations of the YTMLR were compared to those of the sunspot number (SSN), X-ray flare flux, and the Disturbance Storm Time (Dst) index. We show that the CME mass included in the CDAW catalog reflects with high accuracy the actual mass-loss rate from the Sun through CMEs. Additionally, it is shown that the CME mass distribution in the log-lin representation reflects the Gaussian distribution very well. This means that the CMEs included in the CDAW catalog form one coherent population of ejections that have been correctly identified. Unlike the CME occurrence rate, it turns out that the YTMLR is a very good indicator of solar activity (e.g., SSN) and space weather (e.g., Dst index) consequences. These results are very important, since the YTMLR, unlike the mass loss through solar wind, significantly depends on solar cycles.

Unified Astronomy Thesaurus concepts: The Sun (1693); Solar activity (1475); Solar storm (1526)

1. Introduction

Coronal mass ejections (CMEs) are sudden expulsions of magnetized plasma from the outer atmosphere of the Sun. The first CME was recorded in 1971 using the seventh Orbiting Solar Observatory coronagraph (Tousey 1973). Using several space-borne coronagraphs, such as the Apollo Telescope Mount coronagraph (MacQueen et al. 1974) onboard Skylab, the Solwind coronagraph (Michels et al. 1980) onboard the P78-1 satellite, the Coronagraph/Polarimeter (MacQueen et al. 1980) onboard the Solar Maximum Mission, and, currently, the Large Angle and Spectrometric Coronagraph (LASCO; Brueckner et al. 1995) onboard the Solar and Heliospheric Observatory (SOHO) mission (Domingo et al. 1995) and the Sun-Earth Connection Coronal and Heliospheric Investigation (Howard et al. 2008) instruments onboard the Solar Terrestrial Relations Observatory (Kaiser et al. 2008), CMEs have been observed (see Gopalswamy 2016 for a historical development of the field). The longest series of observations continues to be obtained by the SOHO/LASCO coronagraphs. The data cover two complete solar cycles (SCs), 23 and 24. The results of these observations are stored, among others, in the Coordinated Data Analysis Workshop (CDAW) catalog (Yashiro et al. 2004; Gopalswamy et al. 2009). This database is based on visual tracking of the fastest structures on LASCO images by human observers. The basic properties of CMEs have been analyzed in several studies (St. Cyr et al. 2000; Gopalswamy et al. 2003a, 2003b, 2004; Yashiro et al. 2004; Gopalswamy 2010a; Howard et al. 2013; Lamy et al. 2019; Lara et al. 2020). As of 2019 December, about 30,000 CMEs were included in the CDAW catalog. These CMEs are employed in this study.

CMEs have been intensively studied because of their significant impact on the Earth's space environment. The severest consequences in solar, interplanetary, and planetary space are caused by extreme events on the Sun. An extreme event consists of a flare with unusually high intensity associated with an extremely energetic CME (Gopalswamy et al. 2005a; Gopalswamy 2009, 2018a). The magnetic fields carried by CMEs can significantly lower the Disturbance Storm Time (Dst) index, indicating geomagnetic storms. Very fast CMEs drive strong shocks that accelerate protons up to GeV energies (e.g., Gopalswamy et al. 2012). These particles, along with the extremely intense high-energy radiation from the flares, penetrate Earth's atmosphere, causing a threat to the technology placed in space. Human society has become increasingly dependent on technology that can be adversely affected by solar energetic events. Therefore, forecasting space weather is now an important issue. This is not an easy task, because the expansions of ejections depend on the magnetic force that drives them (the physical conditions in the Sun) and the conditions prevailing in the interplanetary medium, as well (Vršnak et al. 2004; Gopalswamy et al. 2014, 2015a; Manchester et al. 2017; Dumbović et al. 2018).

This study is focused on a statistical analysis of the masses of CMEs, based on LASCO observations in the time period 1996–2019 (over two SCs, 23 and 24). White-light coronagraphs record the photospheric light scattered by the coronal electrons, and therefore allow us to measure the coronal density and mass of CMEs (Poland et al. 1981). The estimation of CME mass involves a number of assumptions (Vourlidas et al. 2000; Colaninno & Vourlidas 2009) and restrictions (Vourlidas et al. 2010). Excluded from the mass determination are events with less than four height–time measurements, as well as overlapping and narrow events (with widths $\leqslant 20°$; Vourlidas et al. (2010)). Vourlidas et al. (2010) conducted a comprehensive error analysis of CME mass calculations. They analyzed

the errors resulting from the adopted assumptions and the individual steps in the analyses of coronagraphic images. It turned out that instrumental effects, the coronal background, and the CME plasma composition generate insignificant errors in mass determination. Only projection effects can significantly affect mass determination. Taking all these factors into account, it can be concluded that the obtained CME masses are approximately underestimated by a factor of 2. Therefore, there are large uncertainties in mass determination. It is probably for this reason that studies of CME masses are very rare. Mishra et al. (2019) considered the mass-loss rate (MLR) through solar wind and CMEs and its relation to the sunspot number (SSN), the solar X-ray background intensity, the latitudinal distribution of CMEs, and the phases of solar cycles. They found that the MLR through CMEs is more correlated with the X-ray background intensity than with the SSN. An important result of this research was that the MLR through solar wind does not depend significantly on solar activity cycles, and is an order of magnitude larger than the MLR through CMEs. Lamy et al. (2019) concentrated on comparisons between the different catalogs. They found that the MLR through CMEs tracks different indicators of solar activity (e.g., the SSN and the radio flux F10.7) with no time lag. They also demonstrated that the distribution of the masses of CMEs significantly departs from a Gaussian shape, suggesting the existence two or more physically different populations of CMEs. Both studies revealed that the MLR reported by the CDAW catalog tracks solar activity very well, unlike the occurrence rate of CMEs.

Since extensive statistical studies are important for minimizing the impact of uncertainty in mass determination, we investigate the MLR through CMEs in the two solar cycles as a function of their masses, widths, or position angles. We also analyze the relation of the MLR to the SSN, X-ray flares, and Dst index. There is a significant discrepancy between the CME catalogs regarding the occurrence rate of CMEs. This concerns especially weak/poor events (see Figure 11 in Lamy et al. 2019). Therefore, we use the average mass of CMEs, but focus on an investigation of the total mass ejected from the Sun in a given period of time (a year, a cycle, or all of the relevant scales).

This paper is organized as follows. In Section 2, we describe the data used for the study. Next, in Section 3, the results of our study are presented. Finally, we summarize the results in Section 4.

2. Data

In our study, we utilize the CDAW database.[4] This database relies on visual identification and tracking of the fastest structures of the CMEs in the LASCO C2 and C3 coronagraph images. The height–time profiles and LASCO images are used to determine the basic attributes of the CMEs —the central position angle (CPA), width, speed, acceleration, mass, and kinetic energy. In the present study, we concentrate on the mass budget due to CMEs. It is necessary to mention that the large amount of data available from the SOHO coronagraphs has encouraged scientists to develop automatic techniques to identify CMEs: the Computer Aided CME Tracking Software (CACTus; Robbrecht & Berghmans (2004), the Solar Eruptive Event Detection System (Olmedo et al. 2008), the Automatic Recognition of Transient Events and Marseille Inventory from Synoptic maps (Boursier et al. 2009, and COR onal IMage Processing (Byrne et al. 2012). Unfortunately, there are large discrepancies, especially in the occurrence rate (by factors of 2–3; Lamy et al. 2019 and references therein), between these databases (Petrie 2015; Lamy et al. 2019). The differences between them are most significant during the last minimum of solar activity between SCs 23 and 24. During this period of time, many slow and narrow events were recorded by the CDAW catalog. Unlike the other catalogs, the CDAW detection rate does not track the solar activity cycles very well. Figure 1 shows the temporal evolution of the yearly occurrence rate of CMEs (YORC; upper panel; from the CDAW catalog) in comparison with the yearly mean total sunspot number (bottom panel; from the Sunspot Index and Long-term Solar Observations).[5] The Pearson correlation coefficient for these parameters is 0.54, which is statistically significant at the confidence level $\alpha = 0.05$.

It is clear that both parameters are significantly correlated, but we can also notice clear differences between them. The most striking feature is that we observe many more CMEs in SC 24 compared to SC 23, despite the fact that the SSN shows the opposite trend. It is to be noted that CMEs can originate not only from active regions, but also from polar crown filaments (PCFs; Gopalswamy et al. 2003a, 2003b), from filament regions outside active regions (Gopalswamy et al. 2018), or from streamers (Vourlidas & Webb 2018; Webb et al. 2018). Recently, Michalek et al. (2019) demonstrated that the enhanced CME detection rate can be simply explained by the evolution of the complex solar magnetic field. It was shown that the occurrence of CMEs is the result of the global evolution of the magnetic field on the Sun, and not only changes in the magnetic structures associated with sunspots. Since 2004, the solar magnetic field has become very complex, with the specific structures of streamer belts and coronal holes, and it has been able to generate many low-energy events. Additionally, these intriguing observations have drawn the attention of scientists not only to the Sun, but also to the conditions prevailing in the interplanetary medium. Gopalswamy et al. (2014, 2015a) suggested that during SC 24 CMEs could easily eject and expand due to the significant decline in total (magnetic+plasma) corona and interplanetary pressure caused by the low and extended last minimum of solar activity (between SC 23 and SC 24). As a result of these two factors (an increase in solar magnetic field complexity and a decrease in total interplanetary pressure), a real increase in the CME rate recorded by the CDAW catalog since 2004 has been observed.

Compared to the manual CDAW database, the automated detection method seems to be more objective in the evaluation of the basic parameters of CMEs (width, speed, or acceleration), but its detection criteria cause concern (Yashiro et al. 2008). Yashiro et al. (2008) compared the identifications of CMEs offered by the CACTus and CDAW catalogs. Their consideration revealed that the SOHO/LASCO catalog probably missed about 2000 narrow CMEs in the beginning phase of LASCO observations (before 2004). During this period, the CDAW catalog was affected by observer bias, since it was compiled by at least four different observers (Webb & Howard 2012) and there were no clear criteria for including or disregarding narrow events. But the CACTus catalog has recorded many false events, since it counts streamer deflections

[4] https://cdaw.gsfc.nasa.gov

[5] https://wwwbis.sidc.be/silso/

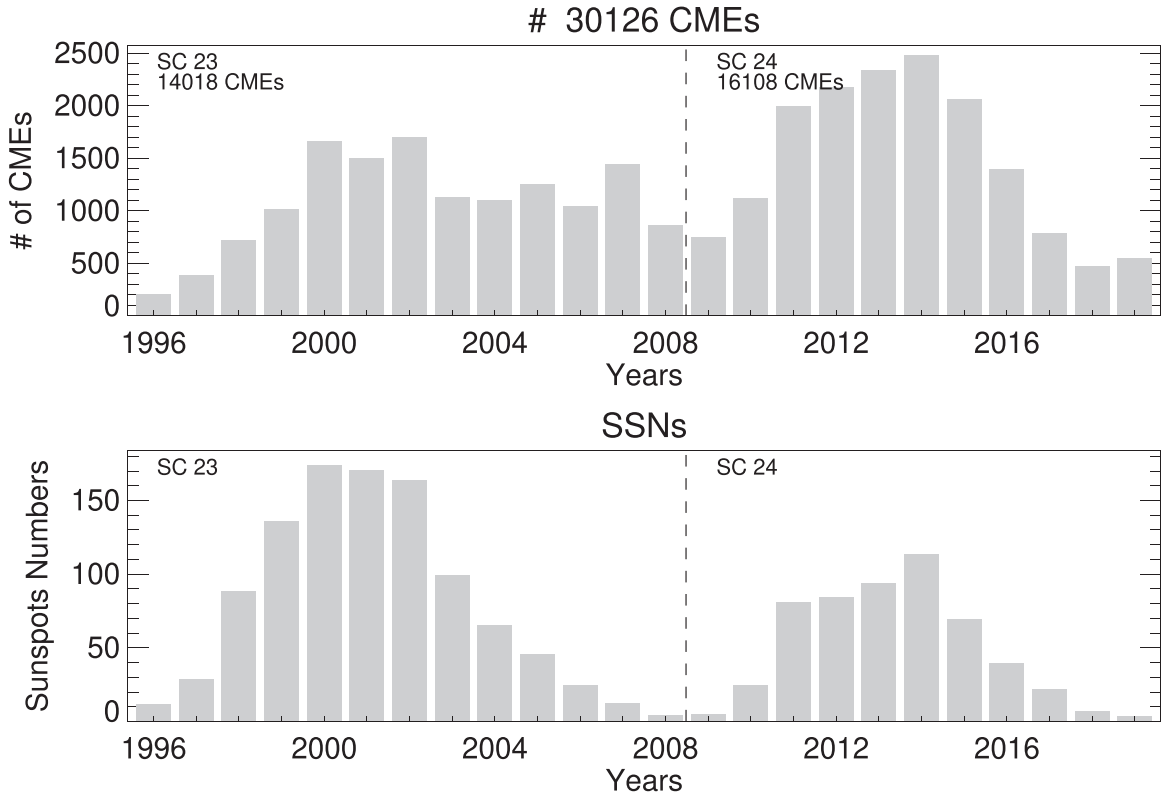

Figure 1. The temporal evolution of the yearly occurrence rate of CMEs (upper panel; from the CDAW catalog) in comparison with the yearly mean total sunspot number (bottom panel; from the Sunspot Index and Long-term Solar Observations). The vertical dashed line separates the two SCs, 23 and 24.

pushed by a large CME or the internal parts of a CME as separate events. These events can constitute up to 30% of the entire CME sample (Vourlidas et al. 2013). It seems that human inspection is the best method for the identification of CMEs (Yashiro et al. 2008; Hess & Colaninno 2017; Vourlidas et al. 2017; Webb et al. 2017). The correct identification of the CMEs is a very important factor in determining their masses, therefore in our study we employ the masses included in the CDAW catalog.

3. Analysis and Results

The Sun loses its mass by two means of mass loss: the solar wind and CMEs. In the present research, we consider only the MLR through CMEs. Because there is a problem with including or disregarding poor events (narrow or weak events), we try to avoid the average mass of CMEs. Instead, we prefer to consider the total mass ejected from the Sun over a given period of time. In order to study the temporal variation of the MLR over SC 23 and SC 24, we use the yearly total mass-loss rate (YTMLR; the yearly sum of the CME masses listed in the catalog). For this purpose, we employ only the masses included in the CDAW catalog. As we mentioned above, the CDAW catalog includes masses for ≈65% of all recorded CMEs. In order to check whether this restriction affects the temporal evolution of the MLR, Figure 2 shows the yearly occurrence rate of all of the recorded CMEs (the continuous curve) and those with known masses (the dashed curve). They track each other very well, and can be matched almost perfectly by multiplying the rate of CMEs with known masses by a factor of 1.53. The correlation coefficient for the occurrence rate is 0.96, so it is very significant. We see that the temporal evolution of the MLR is not affected by the CME detection rate, so our considerations should be correct. The results of this study are presented in the following sections.

3.1. Total Mass-loss Rate

As we demonstrated above, the CME detection rate does not follow the SSN very well. This is due to the increase in the occurrence rate of narrow and poor events since 2004. We can assume that these CMEs are not very massive, therefore their contribution to the total mass lost from the Sun is negligible. Figure 3 displays the temporal evolution of the YTMLR through CMEs. At the top of the figure, the total mass loss (TML) during the entire period of time considered is given (2.99e+19g). Additionally, the TMLs in individual cycles are presented in Figure 3. The YTMLRs are expressed as fractions of the TMLs (2.99e+19g). This means that, on average, the Sun ejects 1.25e+18g plasma through CMEs per year. Because the catalog misses mostly poor events (events with less than four height–time measurements, and overlapping and narrow events), this is only the lower limit on the MLR. For the Sun, this MLR is completely negligible. Assuming that this rate is constant over the Sun's evolutionary timescale, we can calculate that the Sun has lost $\approx 10^{-6}$ of its mass over its lifetime.

Figure 3 also revealed that the YTMLR tracks the SSN much better than the CME detection rate. The correlation coefficient between the SSN and the YTMLR is 0.86. But still this correlation is not perfect. Although we observe a decrease in the YTMLR in SC 24 compared to SC 23, this decrease is not as significant as in the case of SSN. Considering only sunspots, it turns out that SC 24 was 35% percent less intense than SC 23. On the other hand, taking into account the TMLs in both cycles, we find that SC 24 (TML = 1.37e+19 g) is only 15% less

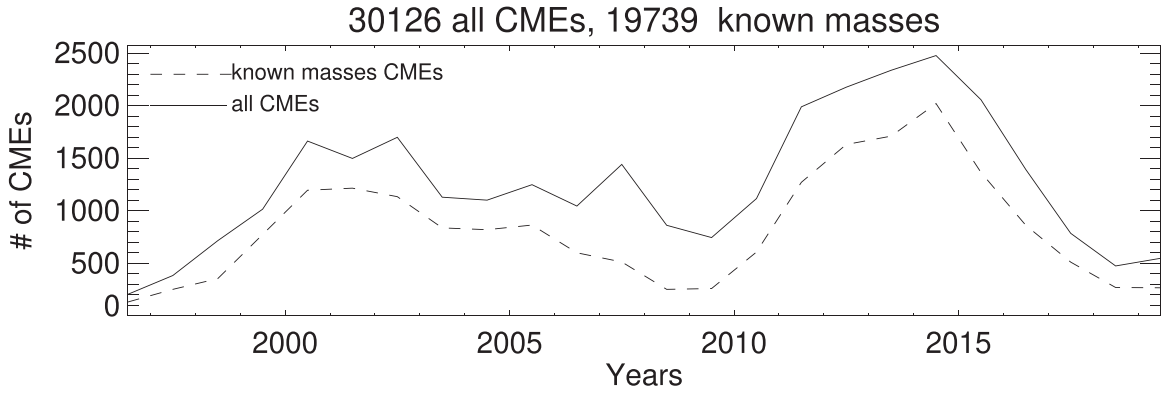

Figure 2. The yearly occurrence rate of all detected CMEs (the continuous curve) and the CMEs with known masses (the dashed curve).

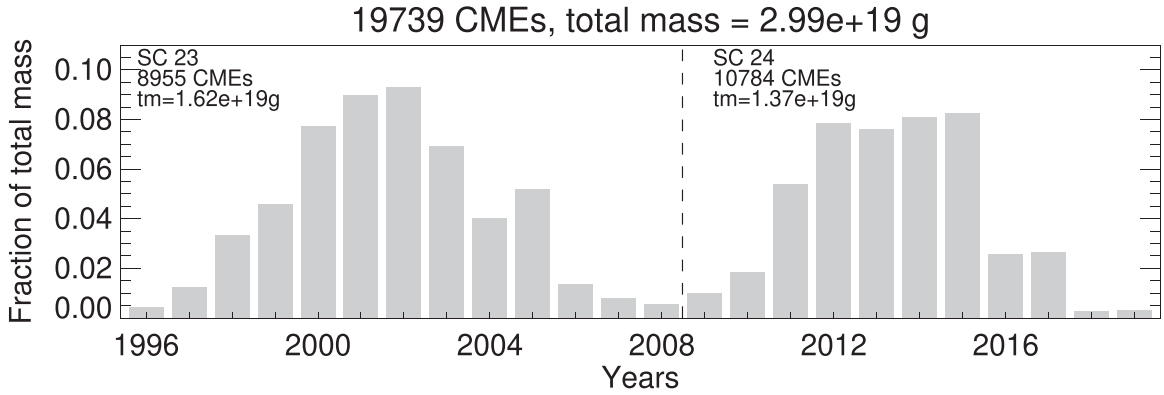

Figure 3. The temporal evolution of the YTMLR through CMEs over SC 23 and SC 24.

pronounced than SC 23 (TML = 1.62e+19 g). It seems that the total mass ejected from the Sun through CMEs in SCs 23 and 24 is very similar. Therefore, we can conclude that the TML from the Sun through CMEs does not depend significantly on cycles of solar activity or the CME occurrence rate. Various types of ejections contribute to the TMLs in both cycles, however. The average mass of all of the ejections is 1.51e+15g, but it was up to 1.81e+15g in SC 23 and only 1.27e+15g in SC 24. SC 24 is characterized by a higher number of events, but on average they were less massive (30% less massive) compared to SC 23. From the figures, we see that the temporal evolution of the YTMLR depends on the phase of a given cycle, and that it differs between cycles as well. In SC 23, we can distinguish a clear peak of the YTMLR (in 2003). So, during SC 23, the YTMLR lagged the sunspot peak by two years. In SC 24, we do not observe a clear maximum in the YTMLR. During this cycle, the YTMLR has a flat maximum covering the period of four years (2012–2015).

3.1.1. CMEs without Determined Mass

As many as 35% of the CMEs in the CDAW catalog are without a known mass. These events were mostly narrow (with angular widths <20°), overlapping, or faint, and could not be tracked in at least four images. Figure 4 displays the distributions of the angular widths of CMEs with determined mass (left panel) and without determined mass (right panel). It is clearly seen that the CMEs without determined mass are very narrow (<width> = 22°). About 9000 of them have an angular width less than 20°. These CMEs, due to the applied criteria, were disregarded for mass determination. Only about 2000 CMEs without a known mass have a larger angular width. CMEs without a determined mass have an average width equal to 22°. On the contrary, CMEs with a known mass have much larger angular widths (<width> = 71°). Using the relation between CME masses and widths, we can estimate the missed mass in the catalog. Figure 5 (left panel) shows scatter plots of $\log_{10}$(mass) versus $\log_{10}$(width) for CMEs with known masses. We see that there is a significant linear correlation between these quantities ($cm^3 = 0.65$). We separately conducted a similar analysis for both solar cycles. No significant differences were observed between these time periods. A similar correlation was also obtained by Gopalswamy et al. (2005b). Using this correlation, we can estimate the masses of the CMEs that were disregarded in the procedure of determining the masses on the basis of coronagraphic images. Taking the width of every CME without a listed mass value and using the correlation between (log) width and (log) mass (y = −1.7+ 0.23*x), we obtain the respective masses of the CMEs. The right panel in Figure 5 displays the mass distribution of the CMEs obtained given these considerations. As we see, the estimated masses of these events are on average very low (2.60e +14 g, which is only 15% of the average mass of the CMEs with known mass). In this population of events, only ≈150 CMEs have masses larger than 1.0e+16 g. Our estimates show that they account for a mass that is only about 9% of the mass contained in the catalog. Although events without known mass constitute quite a large population of all of the identified CMEs, they do not make a significant contribution to the total mass ejected from the Sun.

3.1.2. Mass-loss Rate versus Mass of CMEs

It is interesting to recognize how the MLR through CMEs is distributed over different masses of ejections. Figure 6 shows the temporal evolution of the YTMLR due to CMEs with different mass ranges (left panels) and the distributions of the angular widths of the CMEs in the respective mass ranges

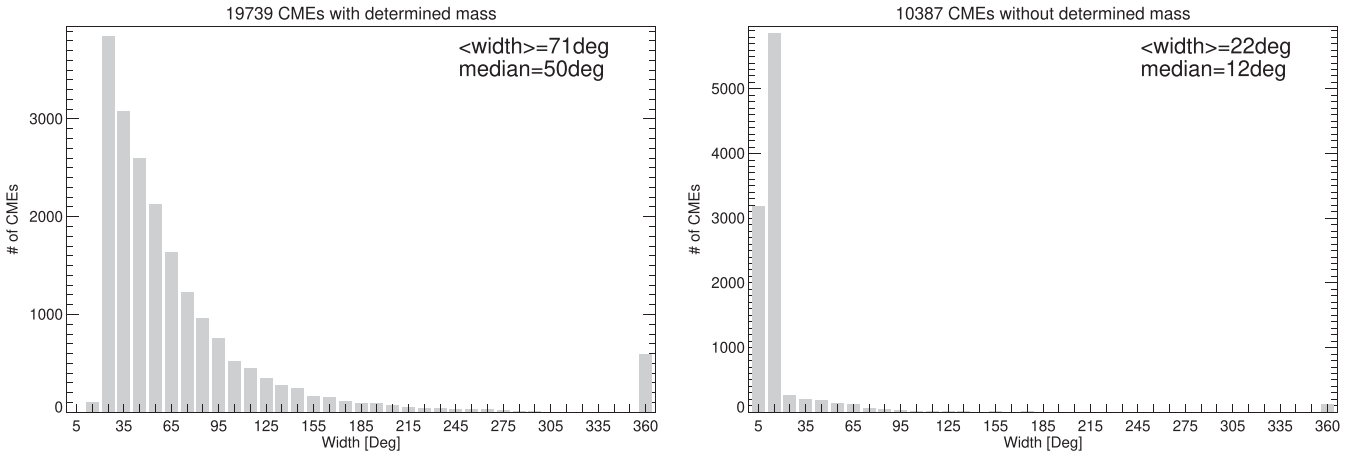

Figure 4. Distributions of angular widths of CMEs with determined mass (left panel) and without determined mass (right panel).

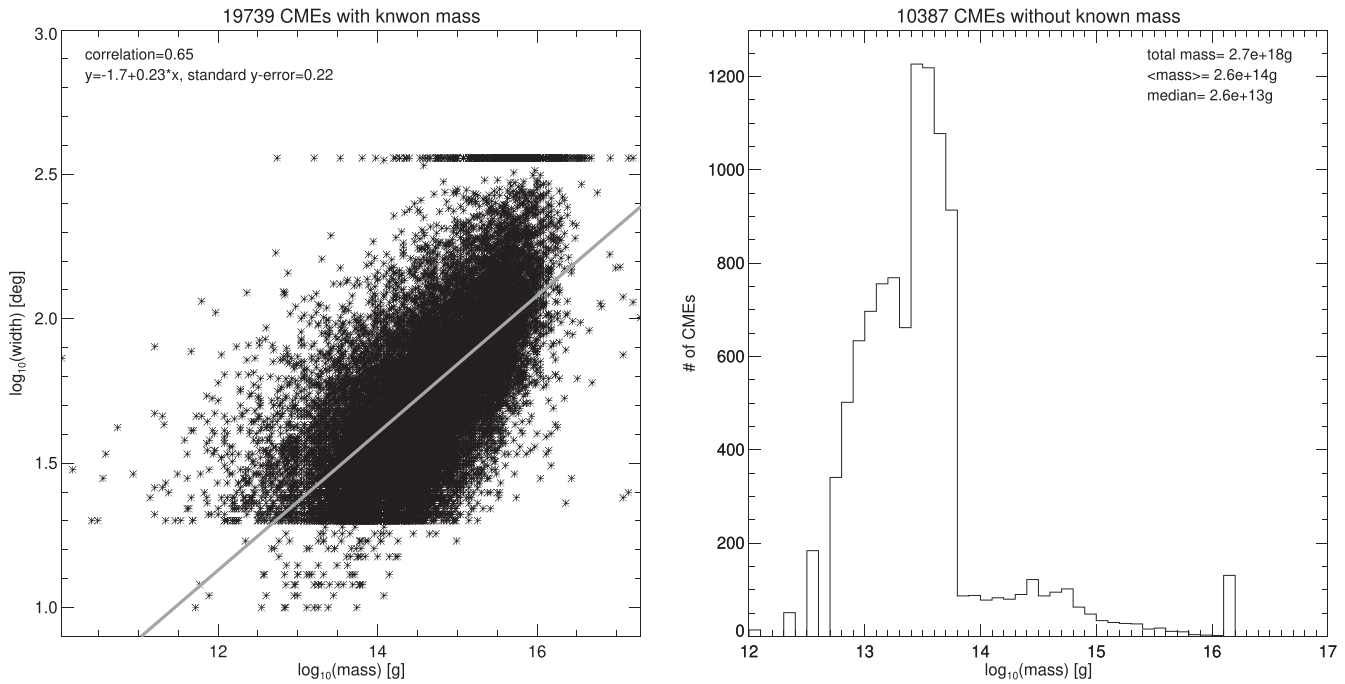

Figure 5. Scatter plot of $\log_{10}$(mass) vs. $\log_{10}$(width) of CMEs with known mass (left panel). Mass distribution of CMEs obtained on the basis of correlation between width and mass (right panel).

(right panels). To show the percentage contribution of the individual CME groups to the total mass ejected from the Sun, the *y*-axis has the same scale as in Figure 3. This scaling is used throughout the article. The mass ranges used for this consideration were chosen arbitrarily, only to show general trends. A first striking feature is the low-mass events (mass $<$ 1.0e+15g), which, despite being the most numerous (14,011), carry only 13% of the total mass ejected from the Sun through CMEs. This means that they do not contribute significantly to the total mass ejected from the Sun. They are also narrower compared to the more massive events. Their average angular width is only 49° (upper right panel). Because the events without known mass (Figure 4) have an average angular width two times smaller than the least massive events, and are of a similar number, we can suppose that they eject even less mass from the Sun compared to these events. Therefore, we can assume that the mass carried by the numerous CMEs without known mass can only contribute 7%–8% to the total mass ejected from the Sun through CMEs. This is similar to the value that we obtained in the previous subsection using the width–mass relationship. This is further confirmation that the CME mass included in the CDAW catalog reflects the actual MLR from the Sun via CMEs with high accuracy.

A second striking feature is that the least frequent, high-mass CMEs (CMEs with masses $>$ 7.0e+15g; bottom left panel) carry a significant part of the total ejected mass (about 41% of the total ejected mass). Almost the same amount of mass is ejected from the Sun through the intermediate-mass CMEs (4834 CMEs with masses between 1.0e+15g and 7.0e+15g; bottom left panel). But these CMEs are much more numerous compared to the high-mass events. As we can see, from the right panels, events with different mass ranges are associated with different populations of CMEs, defined by their widths. The low-mass events are mostly associated with the narrowest CMEs, but the high-mass events are generally wide and are

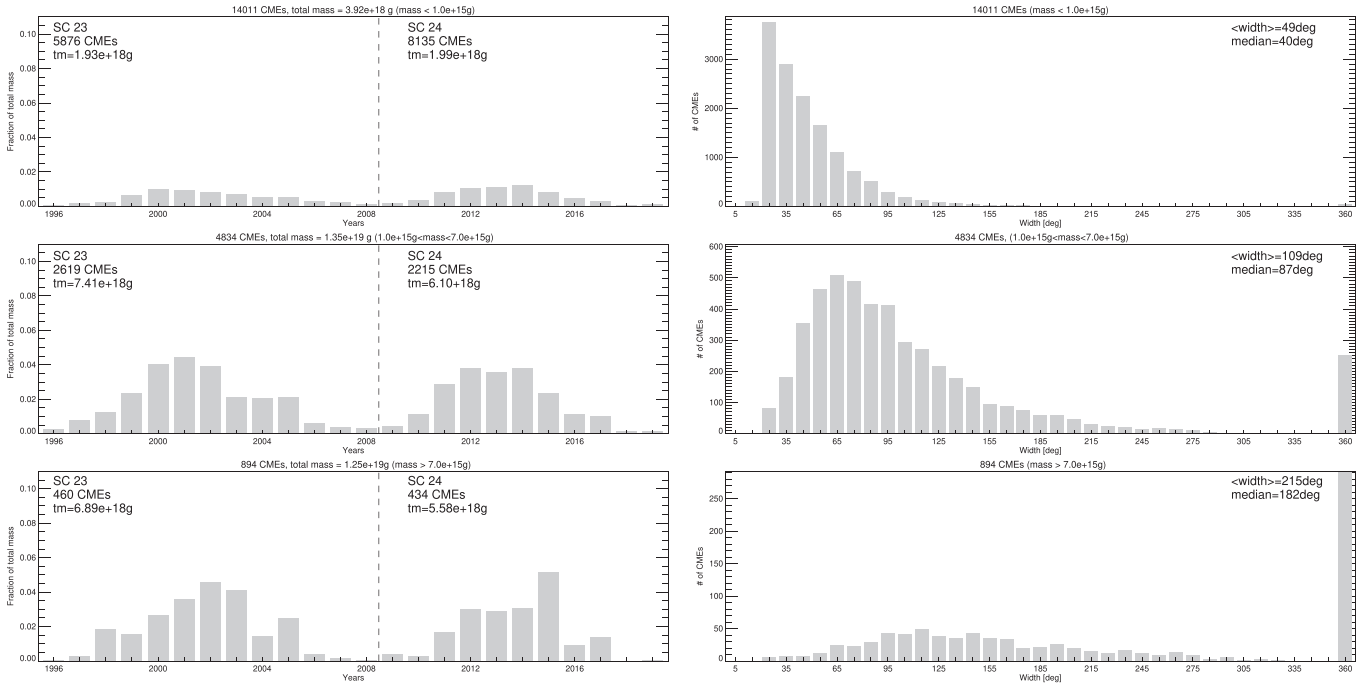

Figure 6. The temporal evolution of the YTMLR due to CMEs with masses lower than 1.0e+15g (upper left panel; low-mass events), between 1.0e+15g and 7.0e+15g (middle left panel; intermediate-mass events), and larger than 7.0e+15g (upper left panel; high-mass events), and distributions of the angular widths of the CMEs in the respective mass ranges (right panels). To show the percentage contributions of the individual CME groups to the total mass ejected from the Sun, the *y*-axis has the same scale as in Figure 3.

dominated by halo events. 75% of the high-mass CMEs are partial (angular width $> 120°$) or halo events. The average angular widths for these three populations of CMEs, divided by mass, differ significantly and are 49° (for the low-mass CMEs), 109° (for the intermediate-mass CMEs), and 215° (for the high-mass CMEs), respectively. It is worth noting that full-halo CMEs (591 with determined mass) carry 22% (5.45e+18g) of the total ejected mass. In SC 23, we recorded 286 halo CMEs with total mass 2.55e+18g, but in SC 24 there were 305 halo CMEs with total mass 2.90e+18g. This means that in both cycles of solar activity, the average masses of the halo CMEs were very similar.

The third striking feature is that the high-mass events eject significantly more mass in the declining phase of maximum solar activity. The largest MLRs, through the high-mass events, are observed in 2002–2003 (SC 23) and in 2015 (SC 24), respectively. The increased MLRs during these periods of time are due to the addition of massive eruptions of PCFs, mostly associated with halo CMEs. This was confirmed by the analysis of polar diagrams and histograms, not presented in the paper, showing the distributions of mass ejected from the various regions of the solar disk and of mass ejected through halo events during different periods of solar activity.

For this reason, the YTMLR through the high-mass events is least correlated with the SSN in comparison to the other samples of CMEs (the correlation coefficient is 0.75). On the other hand, the YTMLR though the intermediate-mass events tracks the SSN almost perfectly (the correlation coefficient is 0.89). This means that such events are associated with active regions. The YTMLR through the low-mass events is also significantly correlated with the SSN (the correlation coefficient is 0.89). In conclusion, we must note that the correlation between the YTMLR and the SSN (the correlation coefficient is 0.86) is much more significant than the correlation between the YTMLR and YORC (the correlation coefficient is 0.54).

3.1.3. Mass versus Angular Width

As we demonstrated in the above section, the masses of CMEs are related to their angular widths. It seems interesting to know how individual events contribute to the total mass ejected from the Sun. Figure 7 presents the distribution (left panel) and the cumulative distribution (right panel) of the MLR though CMEs with different widths. This figure reveals that the most pronounced contributions to the TML (60%) are due to CMEs having angular widths in the range from 50° to 120° and halo events. A very interesting result of this study is that the halo events, which make up only 2.5% of all of the recorded CMEs, carry up to 20% of the total mass ejected from the Sun. This result may be somewhat confusing. It would seem that most of the mass is ejected by events directed toward the Earth. Obviously this is impossible, as the Sun generates ejections randomly. It turns out that halo CMEs can be located at any solar latitude (Gopalswamy et al. 2015a). They can even arise at the edge of the solar disk. As such, in order to be observed around the entire occulting disk as halo events, they must be extremely wide and fast. It is known that the CME halo population is, above all, wide and extremely energetic (Gopalswamy et al. 2015a). They are also geoefficient (directed toward the Earth), because their angular widths are large and they usually interact with the Earth's magnetosphere. The remaining mass is carried out by partial halo events ($120° <$ angular width $< 359°$; about 20% of the TML).

3.1.4. Mass versus Position Angles

The latitudinal location of a CME is given by the CPA. The CPA is defined as the mid-angle between the two side edges of

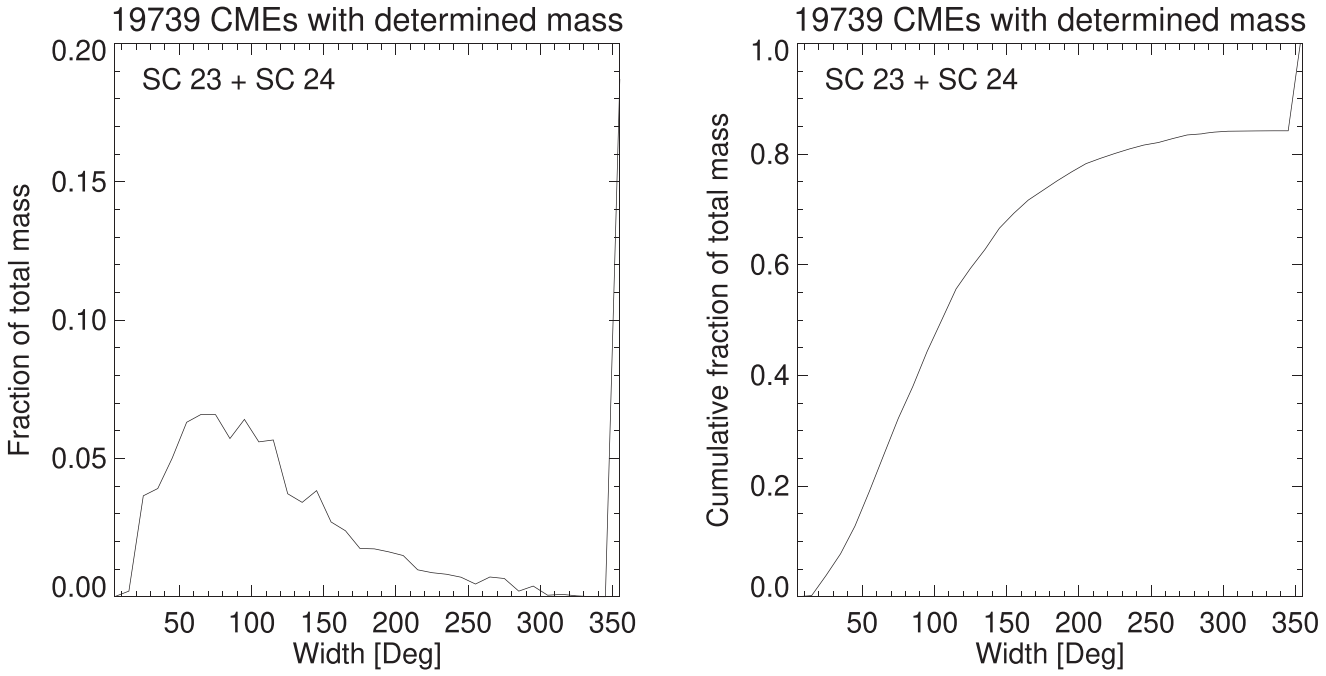

Figure 7. Distribution (left panel) and cumulative distribution (right panel) of the MLR through CMEs with different angular widths.

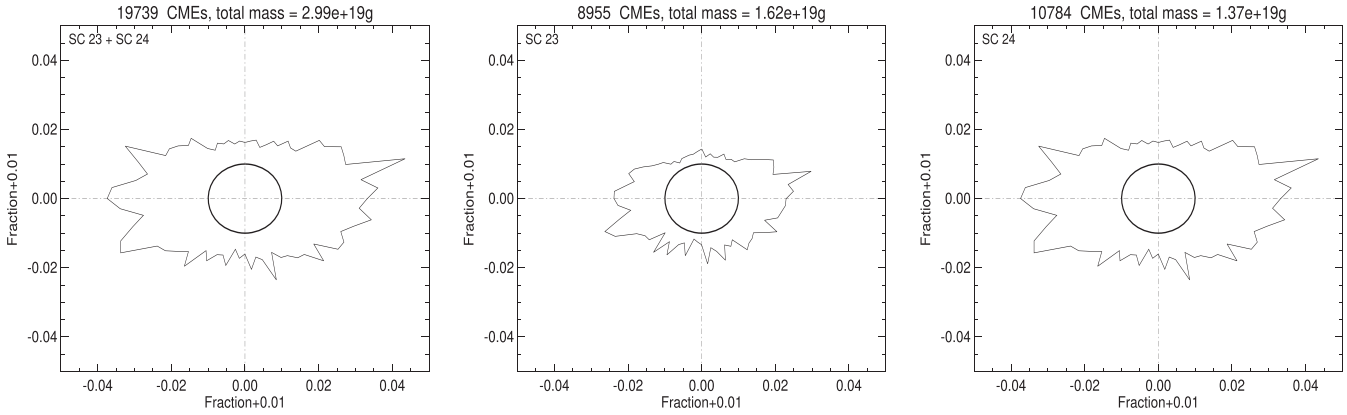

Figure 8. Polar diagrams showing distributions of the TMLR for the three periods of time: 1996–2019 (SC 23+SC 24; left panel), 1996–2008 (SC 23; middle panel), and 2009–2019 (SC 24; right panel). The polar diagrams show the fraction (expressed in the TML = 2.99e+29erg) of the TMLR in 5° PA bins. The central circle represents the Sun.

the CME in the sky plane. The position angle (PA) is measured counterclockwise from Solar North in degrees (from 0° to 360°). Unfortunately, for halo events, the CPAs cannot be determined. In our study, the locations of the halo CMEs were obtained from the base of the PA at which the height–time measurements were made. The measurement position angle and CPA are very close to each other, and can be used interchangeably. Figure 8 shows the polar distribution of the total mass-loss rate (TMLR) in 5° CPA bins for the three considered periods of time (SC 23+SC 24, SC 23, and SC 24). As expected, the TMLR is very significant in a wide belt surrounding the solar equator. This belt, however, is not limited to solar latitudes where active regions appear, but extends up to 60° from the solar equator (to areas where PCFs are observed). This belt is clearly seen for both cycles (SC 23 and SC 24). The low-mass ejection rate is recorded in areas close to the solar poles. Figure 9 shows similar polar diagrams, but separately for SC 23 (upper panels) and SC 24 (bottom panels), and the low-mass (left panels), intermediate-mass (middle panels), and high-mass (right panels) events. Despite the fact that they are the most numerous, the low-mass CMEs contribute very little to the mass carried by CMEs from the Sun. As can be seen from Figure 9 (left panels), in both cycles of solar activity, the low-mass CMEs mostly carry the mass in a wide belt around the solar equator. The intermediate-mass events contribute significantly to the total mass ejection from the Sun (middle panels). It is clear that during SC 23 these CMEs mostly carry mass from the central streamer belt. During this time, the most intensive mass loss through the intermediate-mass events is from close to the equator (this corresponds to ≈90° and ≈270° in PAs). On the other hand, during SC 24, the MLR through such events is not so closely concentrated on the central streamer. During this solar cycle, the global solar magnetic field was very complex (Michalek et al. 2019): two streamer belts, shifted about 20° to the north and south of the solar equator, were formed. Therefore, as we can see (bottom middle panel), the MLR through intermediate-mass events was mostly distributed in a wide belt (up to ±50° for solar latitude) around

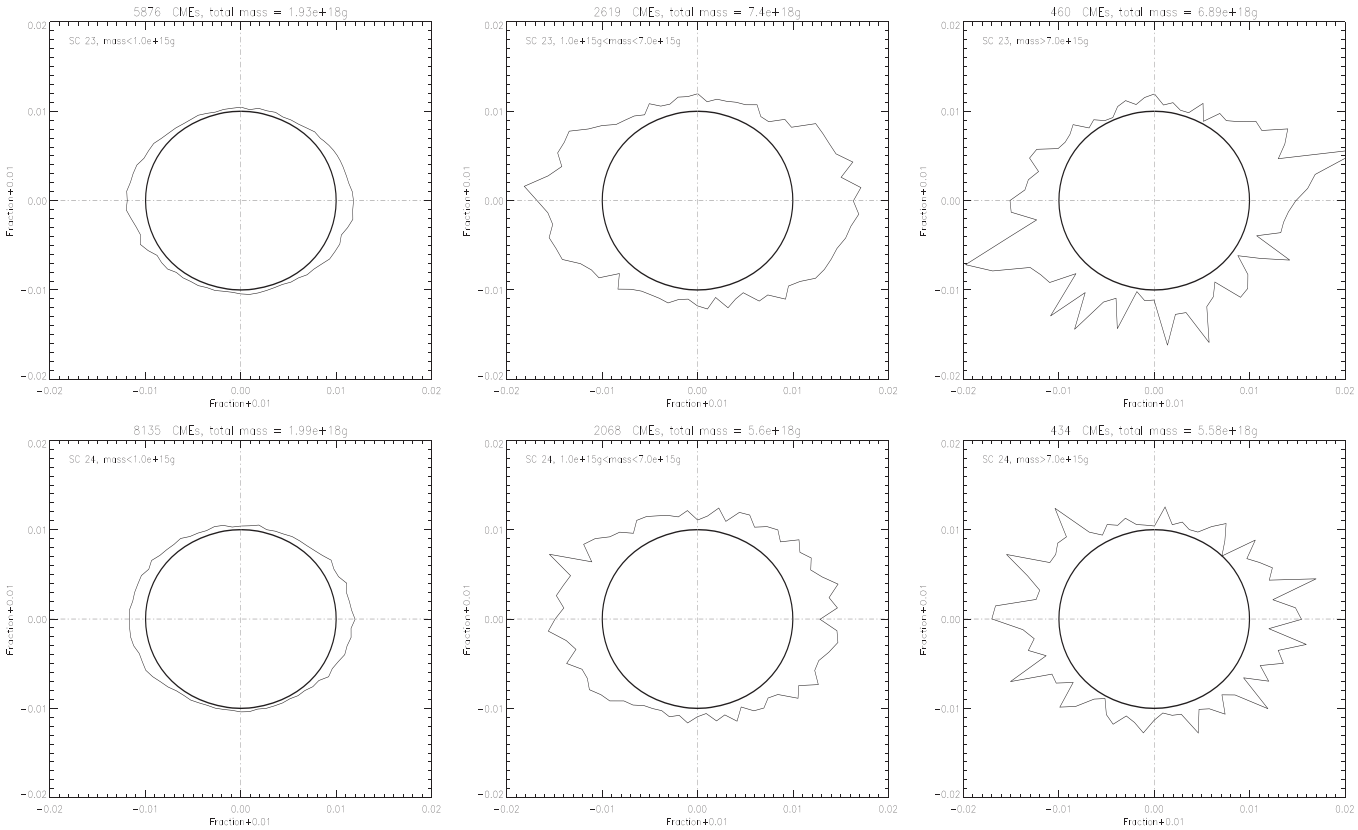

Figure 9. Polar diagrams showing distributions of the TMLR for the two solar cycles separately (SC 23: top panels; SC 24: bottom panels), and the low-mass (left panels), intermediate-mass (middle panels), and high-mass (right panels) events. The polar diagrams show the fraction (expressed in the TML = 2.99e+29erg) of the TMLR in 5° PA bins. The central circle represents the Sun. Please note that in the current figure the scale has been reduced compared to Figure 8.

the solar equator. The biggest difference between the cycles is observed for the high-mass events (Figure 9, right panels). In SC 24 (bottom right panel), the high-mass events carry mass from the Sun almost homogeneously around the entire solar disk, with a slight increase in the areas around the solar equator. In the case of SC 23 (upper right panel), we observe two prominent peaks of the MLR (at PAs ≈105° and ≈295°) through the high-mass CMEs. These peaks appeared due to events in the late solar maximum phase and the early declining phase from 2002 to 2004. The mass loss from these regions on the Sun was related to the prominent and stable streamer belt that appeared in this phase of the solar cycle. The streamer belt was significantly inclined to the solar equator. It seems that the polar distributions of the TMLR mimic the structures of the streamers, especially for the high-mass events. This is obviously in line with the prediction, because the helmet streamers are areas with closed magnetic lines where CMEs can be generated. This figure also shows that the high-mass CMEs in SC 23 mostly carry mass from the southern solar hemisphere ($90° < PA < 270°$). This may mean that the mass is ejected asymmetrically from both hemispheres (the northern and southern hemispheres). This asymmetry is largely due to the extreme CMEs generated primarily by the two super active regions 486 and 808 (Gopalswamy et al. 2006). Another interesting detail is observed in the bottom middle panel. This polar diagram shows an excess of northern polar crown eruptions compared to those observed in the southern crown polar. In SC 24, there were polar crown eruptions over a 4 yr period in the north, but over a much shorter interval in the south, based on Nobeyama/Solar Dynamic Observatory prominence observations (Gopalswamy et al. 2016).

3.1.5. North–South Asymmetry

The existence of the north–south asymmetry has been demonstrated by studying several solar activity indicators (Chowdhury et al. 2013; Deng et al. 2017). This asymmetry is crucial to better understanding subphotospheric flows and solar dynamo action. A nonaxisymmetric flow component is necessary to maintain dynamo action on the Sun (Sokoloff & Nesme-Ribes 1994; Moss et al. 2008). Therefore, it is very important to study solar activity indicators for the two hemispheres separately, avoiding blurring this effect in observational data. An analysis of the occurrence rate of CMEs per hemisphere showed a similar asymmetry (Lamy et al. 2019). Considering all of the CMEs with determined mass during both solar cycles, on the basis of the CDAW catalog, the northern and southern CME amounts are 51% and 49%, respectively. So there is only a slight excess of northern CMEs. Considering the two solar cycles separately, the percentages are 0.47% versus 0.53% for SC 23 (an excess of southern events) and 0.54% versus 0.46% for SC 24 (an excess of northern events), respectively. However, we have to point out that the obtained differences, according to the Kolmogorov–Smirnov test, are not statistically significant. It is known that this north–south asymmetry can change during a solar cycle (e.g., Zolotova & Ponyavin 2006; Carbonell et al. 2007). In different phases of the solar cycle, different hemispheres can be more active. Figure 10 shows the temporal evolutions of the yearly

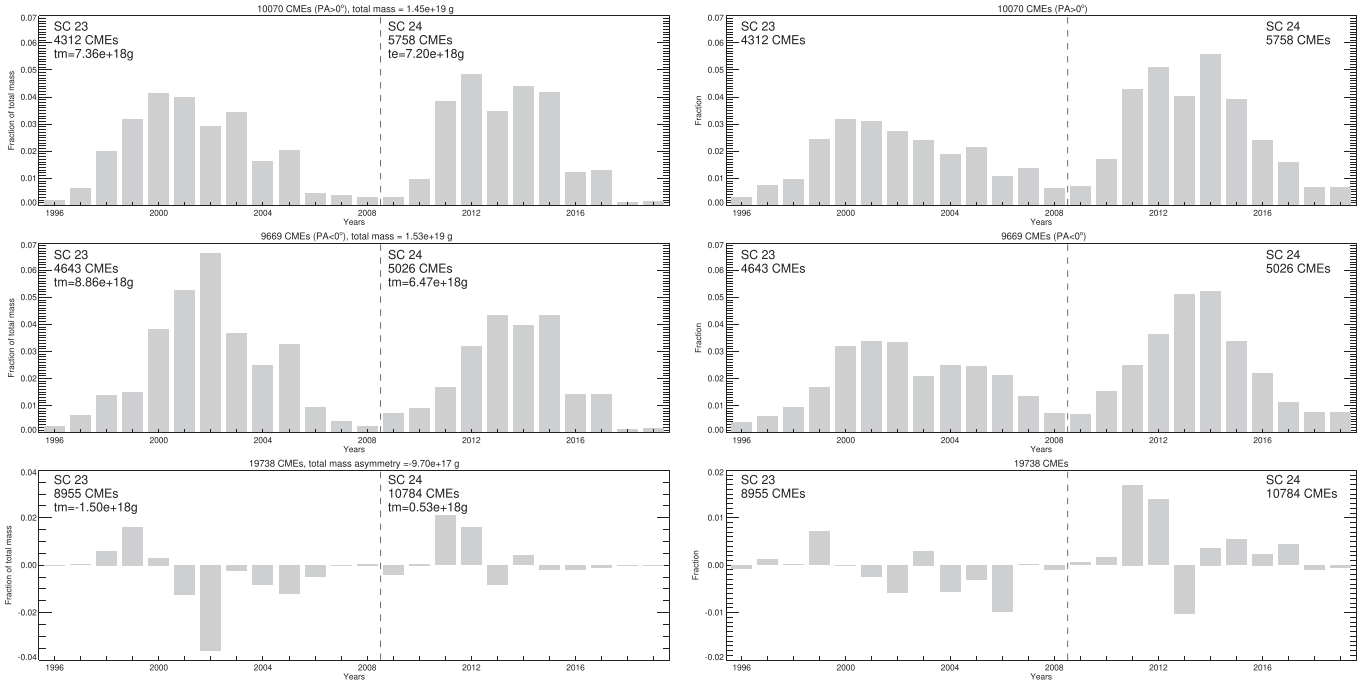

Figure 10. The temporal evolution of the yearly TMLR due to CMEs originating in the northern (upper left panel) and southern (middle left panel) hemispheres, and the difference between them (northern—southern; bottom left panel). For comparison, in the panels on the right, the identical temporal evolutions for the yearly occurrence rates of the respective CMEs are shown. "Fraction" means the ratio of the number of CMEs in a given year to the total number of events.

TMLR through CMEs originating from the northern (upper left panel) and southern (middle left panel) hemispheres, and the difference between them (bottom left panel), respectively. For comparison, in the panels on the right, we present the same distributions, but for the yearly occurrence rates of the respective CMEs. We find that in SC 23, the northern hemisphere initially dominates in the rising phase, but near the maximum of these cycles the southern hemisphere MLR exceeds the northern one and dominates until the end of the cycle. As a result, in the whole of SC 23, significantly more mass was ejected from the southern hemisphere compared to northern one (about 8% more in comparison to the total mass ejected during this cycle). In SC 24, the situation is slightly different. Again, in the rising phase, the northern MLR exceeds the southern one. It was found that, except for Solar Cycle 18, the northern hemisphere dominates during the rising phase (Chowdhury et al. 2019). We also observe, near the maximum of this cycle, the changing of the more active hemisphere from the northern to the southern one. But this is only for a short period of time (2013). This issue is discussed in detail by Gopalswamy et al. (2016). In 2014, the more active hemisphere returned to being the northern one. As a result, over the whole of SC 24, more mass was ejected form the northern hemisphere compared to the southern one. This difference was only 6% of the total mass ejected during this cycle. Considering SC 23 and SC 24 together, we find that about 9.7e+17 g more mass was ejected from the southern hemisphere compared to northern one. This is about 3% of the TML over the two SCs. The opposite result was obtained in the case of the occurrence rate of the CMEs. Over the whole period of time considered, 401 more CMEs (about 2% of all of the considered CMEs) with determined mass originated from the northern hemisphere compared to the southern one. The north–south asymmetry in terms of the mass ejected from the Sun very well follows a similar asymmetry determined on the basis of the SSN (Chowdhury et al. 2013; Deng et al. 2017).

3.1.6. Mass Distribution

An important question concerns the CME mass distribution. Lamy et al. (2019) suggested that the CME mass distribution does not follow a log-normal distribution (Figures 12 and 13 in Lamy et al. 2019), which is manifested in many solar processes (Aoki et al. 2004; Abramenko & Longcope 2005). They stated that CMEs must consist of two or more populations of events distinguished on the basis of their physical properties (e.g., speed). Unfortunately, they arbitrarily excluded "poor" events —which amount to 26% of the total population—from their considerations. Lamy assumed that CMEs flagged as "poor" events in the CDAW catalog are very small or faint, or that they fade out rapidly with height. But this is not true. In the text file for each CME, a quality index is given, which only determines the quality of the coronagraphic images used to obtain the height–time points. This means that many of these "poor" events have determined mass and cannot be omitted from further consideration. A log-normal distribution is a Gaussian distribution on the plot, with the horizontal axis in logarithmic scale and the vertical axis in linear scale. Aoki et al. (2004) suggested that the physical quantities associated with mass outflows demonstrate log-normal distributions, whereas those related to surface emissions show scale-free distributions, such as power-law and exponential distributions. They explained this effect by the filtering process during mass ejection (i.e., filtering favors more energetic events). Figure 11 shows histograms of the CME mass distributions (continuous lines) in log-lin representation (using a bin of 0.1). The left panel is for the two solar cycles, and the middle and right panels are for SC 23 and SC 24, respectively. The dashed line is a Gaussian fit to the histogram. In the upper left corner, there are: the height of the Gaussian fit, the center of the Gaussian fit, the

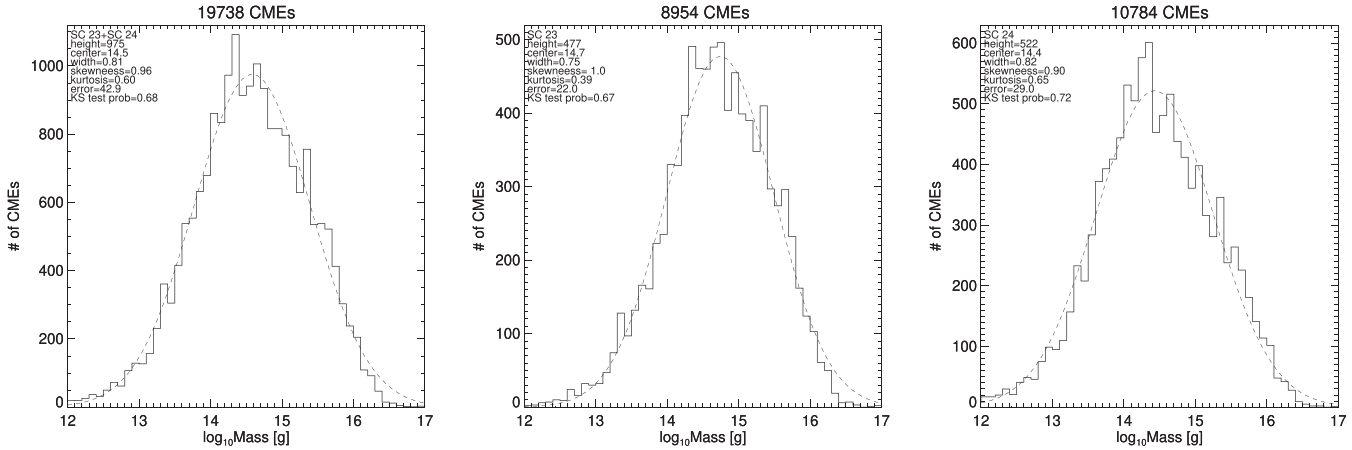

Figure 11. Histograms of the CME mass distributions (continuous lines) in log-lin representation (using a bin of 0.1). The left panel is for the two SCs, and the middle and right panels are for SC 23 and SC 24, respectively. The dashed line is a Gaussian fit to the histogram. In the upper left corners, there are: the height of the Gaussian fit, the center of the Gaussian fit, the width of the Gaussian fit, the skewness of the histogram, the kurtosis of the histogram, the standard error between the histogram and the Gaussian fit, and the Kolmogorov–Smirnov probability that the histogram has a Gaussian distribution.

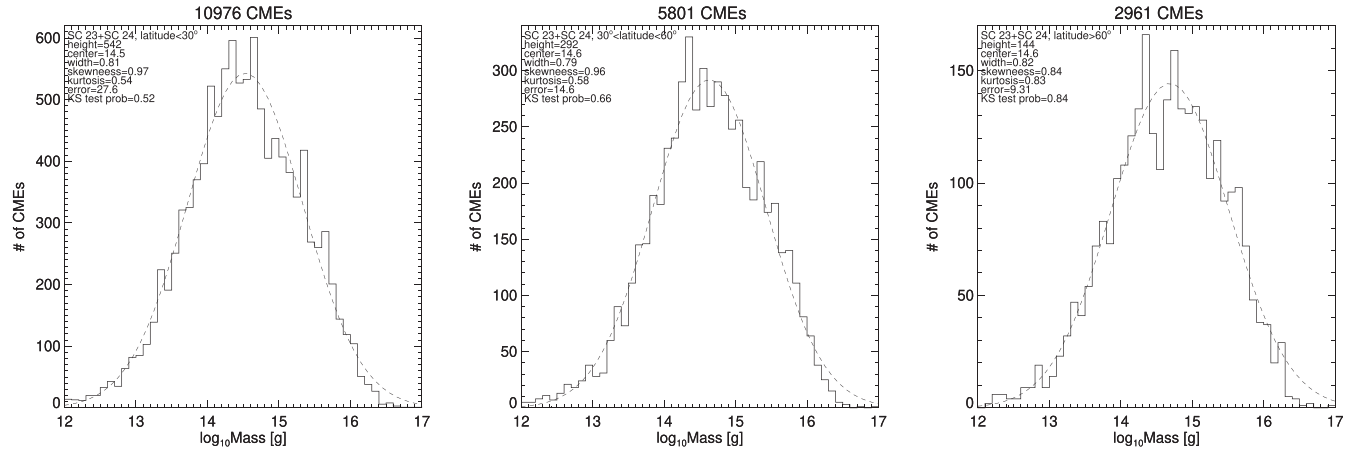

Figure 12. The same as Figure 11, but for CMEs included in the CDAW catalog having different ranges of solar latitudes (latitude $\leqslant 30^\circ$ (left panel); $30^\circ <$ latitude $\leqslant 60^\circ$ (middle panel); and latitude $>60^\circ$ (right panel)).

width of the Gaussian fit, the skewness of the histogram, the kurtosis of the histogram, the standard error between the histogram and the Gaussian fit, and the Kolmogorov–Smirnov probability that the histogram has a Gaussian distribution. From the presented figure, it is clearly seen that the CME mass distribution in the log-lin representation reflects the Gaussian distribution. Such parameters as skewness or kurtosis have very low values. Additionally, the standard error and the Kolmogorov–Smirnov test show that there is a significant agreement between the real mass distributions and the Gaussian distributions fitted to them. This significant agreement occurs for all ejections included in the CDAW catalog (left panel), as well as for events occurring in the last two cycles of solar activity (SC 23: middle panel; SC 24: right panel). On the basis of the presented figure, we can state that the CMEs included in the CDAW catalog form one coherent population of ejections, and that their identification is correct. Of course, we can create subsamples of events by imposing limits on their physical parameters (e.g., speed or angular width). Then, the distributions of their physical parameters may differ from the normal distribution. But these deviations would only be related to the selection criteria. However, it is intriguing whether the mass distribution depends on the solar latitude. CMEs with different latitudes can have different sources of origin. Close to the solar equator, they are likely to originate from active regions; at intermediate latitudes, they can be associated with PCFs; and near the poles, they frequently appear as jets associated with coronal holes. Figure 12 displays the mass distributions for CMEs originating from different ranges of latitude (from areas close to the solar equator, from middle latitudes, and from areas close to the solar poles). Also, in this case, for all of the subsamples of CMEs, we do not observe significant deviation from the normal distribution fitted to them. It is noteworthy that all of the parameters of the Gaussian fits are almost identical, even the centers of curves (the center of a Gaussian fit reflects an average value for a given quantity).

3.2. X-Ray Flares and Mass

It is well known that CMEs are associated with flares and prominence eruptions (Munro et al. 1979). This fact cannot be surprising, because CMEs and flares originate in closed magnetic fields and are different manifestations of the same free magnetic energy release. Kahler (1992) demonstrated that 40% of CMEs have association with H-alpha flares. The CME association rate clearly increases with the peak of X-ray flare intensity (Yashiro et al. 2006). Figure 13 shows the temporal

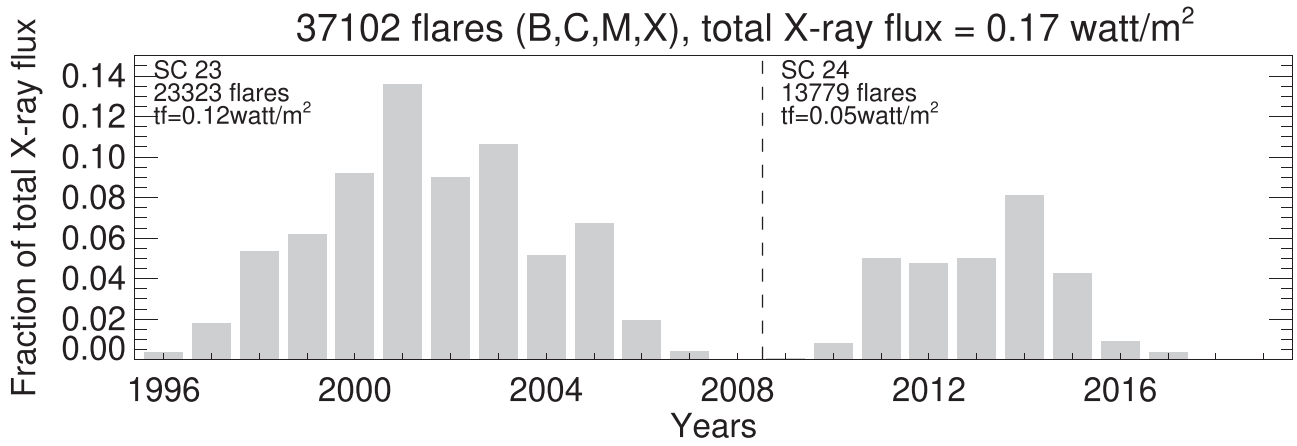

Figure 13. The temporal evolution of the YTXPF of solar flares.

evolution of the yearly total X-ray peak flux (YTXPF; 1–8A) of solar flares. The YTXPF is the sum of the X-ray peaks of all of the flares occurring in a given year. Over almost two solar cycles, the total X-ray peak flux emitted from the Sun is 0.17 W m^{-2}, with as much as 0.12 W m^{-2} (70%) being emitted in SC 23. Regarding this parameter, SC 24 was more than two times weaker, compared to SC 23. We see that the YTXPF follows the SSN very well.

Table 1 displays the linear Pearson correlation coefficients for the parameters considered in this study (SSN: Figure 1; YORC: Figure 1; YTMLR: Figure 3; and YTXPF: Figure 13). We perform a test of the significance of the correlation coefficients. For the Pearson correlation coefficient, at the significance level $\alpha = 0.05$, there is sufficient evidence to conclude that there is a significant linear relation between all of the parameters included in the table. However, it should be noted that the smallest correlation exists between the YORC and YTXPF ($cm^3 = 0.48$). This means that CMEs are different phenomena than flares, and frequently they appear without any flare signature on the Sun. The correlation between the YORCs and the SSN is not much higher ($cm^3 = 0.54$). We find the best correlation between the SSN and YTXPFs ($cm^3 = 0.90$). It is important to note that the YTMLR is very well correlated to all of the other considered solar activity indicators (cm^3 is more than 0.78 for all of them). From this point of view, the YTMLR seems to be the most universal indicator of solar activity.

Figure 14 shows the temporal evolution of the YTXPF of solar flares, but for the four classes of X-ray flares separately (B, C, M, and X). Despite the fact that they are very numerous, class B flares do not make any significant contribution to the total X-ray peak flux of flares (their total contribution is only 4%). The other three classes of flares (C, M, and X) make an almost identical contribution to the total X-ray peak of solar flares (each contributes about 30%). It is also noteworthy that the small number (171) of X-class flares contribute as much as the more numerous C- (20,719) and M-class (2144) flares. It is also clearly seen that SC 24 is much weaker compared to SC 23 in terms of the number of flares (this applies separately to all of the four classes), as well as the total X-ray peak flux of flares. However, for the most energetic class of flares (the X class), the differences between the cycles are the most significant. In SC 24, compared to SC 23, we observe only one third of the X-class flares, and their total X-ray peak flux is four times smaller. Table 2 gives correlation coefficients between the YTMLRs of the different CME categories and the YTXPFs for

Table 1
Correlation Coefficients between the Solar Activity Indicators Considered in This Study

	SSN[a]	YORC[b]	YTMLR[c]	YTXPF[d]
SSN	1.00	0.54	0.86	0.90
YORC	0.54	1.00	0.78	0.48
YTMLR	0.86	0.78	1.00	0.86
YTXPF	0.90	0.48	0.86	1.00

Notes.
[a] Sunspot number.
[b] Yearly occurrence rate of CMEs.
[c] Yearly total mass-loss rate.
[d] Yearly total X-ray peak flux of flares.

the different classes of X-ray flares. From the table, we can notice that the B-class flares are not related to mass ejections from the Sun. In this case, correlation coefficients are not significant. This is not surprising, as only the less numerous CMEs associated with the PCF eruptions could be associated with weaker flares (Gopalswamy et al. 2015b). The best correlation is found between the C- and M-class flares and the yearly MLR of the medium-mass CMEs ($cm^3 \approx 0.90$). This is not surprising, because both of these phenomena, e.g., the flares of the C and M classes and the intermediate-mass CMEs (Figure 5), are the most significantly correlated with the SSN. It is also known that these classes of flares are not only correlated with CMEs from sunspots, but also with events from nonsunspot regions (Gopalswamy et al. 2010). It must also be noted that these two classes of flares (M and C) have the best correlations with all of the groups of CMEs considered here (the correlation coefficients are $\geqslant 0.79$). Another interesting result is that the most energetic flares (the X class) are only moderately correlated with the most massive CMEs ($cm^3 = 0.60$). This means that many massive CMEs must also be related to the PCFs.

3.3. Mass and Geoeffectiveness

CMEs are the major cause of geomagnetic storms, especially those intensive storms with a Dst index lower than −100 nT. The Dst index reflects the enhancement of the ring current encircling the Earth (Takahashi et al. 1990). It is widely used in space weather studies. On this basis, we can determine the

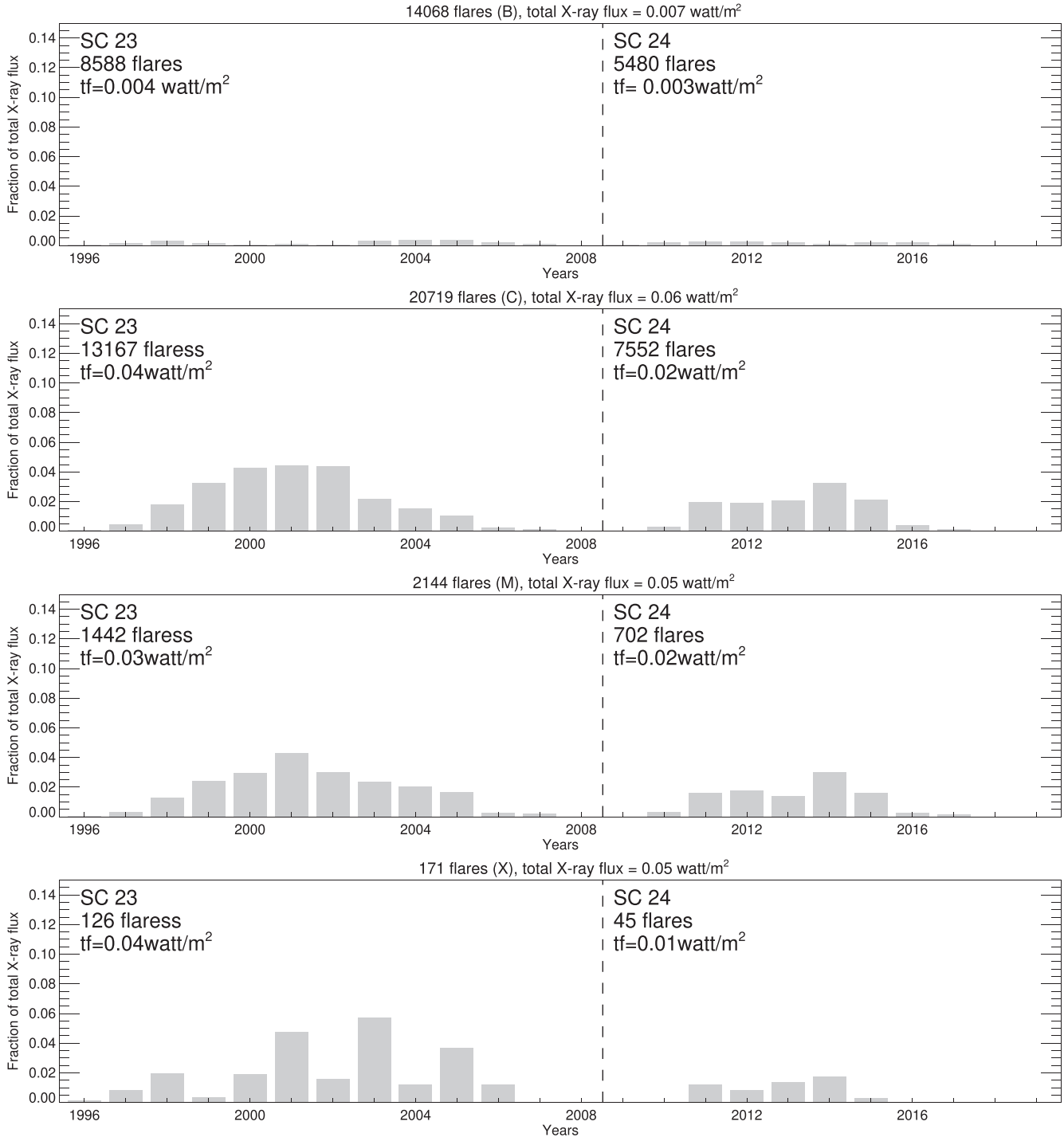

Figure 14. The temporal evolution of the YTXPF of solar flares, for the four classes of X-ray flares separately (B, C, M, and X). For the *y*-axis, we keep the scale from Figure 12.

relationship between the TMLR and the intensities of geomagnetic disturbances. Figure 15 shows the temporal evolution of the yearly mean Dst index (YMDI). As was shown also in a previous study (Gopalswamy 2018b), it mimics the cycles of solar activity. According to the Dst index, SC 24 was on average 35% weaker compared to SC 23. It is remarkable that the lowest YMDI is observed in the final phases of the maxima for both cycles (2003 in SC 23 and 2015 in SC 24). Table 3 displays the linear Pearson correlation coefficients between the YMDI (Figure 4) and the indicators of solar activity considered in the study (SSN: Figure 1; YORC: Figure 1; YTMLR: Figure 3; and YTXPF: Figure 13). First, we should mention that the YORC is not correlated with the YMDI ($cm^3 = -0.19$). This is obviously due to the fact, described earlier in this article, that since 2004 there have been a lot of low-energy CMEs that do not generate any geoeffective activities. The next interesting thing is that the YTXPF could be the best indicator of solar geoeffectivness ($cm^3 = -0.80$), better than the SSN ($cm^3 = -0.72$). The third finding is that the YTMLR, unlike the YORC, is a very good indicator of the YMDI ($cm^3 = -0.66$). Of course, the mean values of the Dst index do not give accurate information about geomagnetic disturbances.

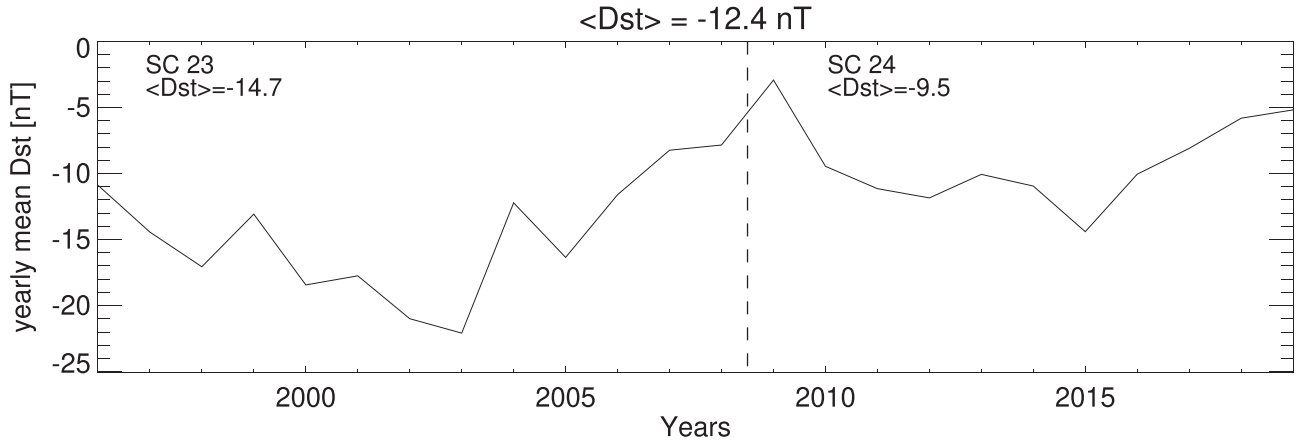

Figure 15. The temporal evolution of the yearly mean Dst index.

Table 2
Correlation Coefficients between the Yearly Total Mass-loss Rate for Different CME Categories and the Yearly Total X-Ray Peak Flux for the Different Classes of X-Ray Flares

	YTXPF[b] B class	YTXPF C class	YTXPF M class	YTXPF X class	YTXPF M+X classes	YTXPF C+M+X classes	YTXPF C+M classes
YTMLR[a] of all CMEs	0.27	0.88	0.88	0.57	0.77	0.86	0.90
YTMLR of the least massive CMEs	0.25	0.80	0.80	0.42	0.64	0.73	0.81
YTMLR of the medium massive CMEs	0.22	0.91	0.90	0.52	0.74	0.85	0.91
YTMLR of the most massive CMEs	0.30	0.79	0.80	0.60	0.74	0.80	0.80

Notes.
[a] Yearly total mass-loss rate.
[b] Yearly total X-ray peak flux of flare.

Table 3
Correlation Coefficients between the Yearly Mean Dst Index and the Solar Activity Indicators Considered in This Study

	SSN[a]	YORC[b]	YTMLR[c]	YTXPF[d]
YMDI[e]	−0.72	−0.19	−0.66	−0.80

Notes.
[a] Sunspot number.
[b] Yearly occurrence rate of CMEs.
[c] Yearly total mass-loss rate.
[d] Yearly total X-ray peak flux of flare.
[e] Yearly mean Dst index.

Therefore, the correlation of the solar activity indicators with geomagnetic disturbances of different intensity should be analyzed as well. According to Loewe & Prölss (1997), with respect to their Dst magnitude, geomagnetic storms are classified into four categories: a geomagnetic storm can be quite minor/weak ($Dst > -50nT$); moderate ($-100nT < Dst \leqslant -50nT$); intense ($Dst \leqslant -100nT$); or severe ($Dst \leqslant -200$ nT). Figure 16 displays the temporal evolutions of fractions of time (in the total considered period of time) when quite minor/weak (upper panel), moderate (middle panel), and intensive (bottom panel) storms were observed. As one might have guessed, the intensity of the geomagnetic disturbances depends on the solar cycles and their amplitudes. The quite minor storms are the most frequent. The moderate and intensive storms are more significantly related to solar activity, and are more frequent during the maxima of SC 23 and SC 24. It is important to mention that, apart from CMEs, fast solar wind streams can also drive corotating interaction regions, and those impacting Earth can cause minor-to-moderate geomagnetic storms (Verbanac et al. 2013). We see also a clear difference between both solar cycles. In SC 23, geomagnetic storms are significantly more frequent compared to SC 24. The largest difference is observed for the most intense storms. In SC 23, they are almost four times more frequent than in SC 24. This was attributed to the dilution of the magnetic content of CMEs due to the backreaction of the weak heliosphere (reduced total pressure; Gopalswamy et al. 2020). Minor differences between the discussed solar cycles are observed for moderate and quite minor storms. This is due to the greater influence of Co-rotating Interaction Regions storms. This is especially noticeable in cycle 24 in 2016 (Selvakumaran et al. 2016). These conclusions find formal confirmation in the results presented in Table 4. Table 4 displays the linear Pearson correlation coefficients for the parameters considered in this study (SSN: Figure 1; YORC: Figure 1; YTMLR: Figures 3 and 5; and YTXPF: Figure 12), and the YMDI is displayed in Figure 15. The first important finding is that the YORC is not significantly correlated with any kind of geomagnetic storm. On the other hand, it turns out

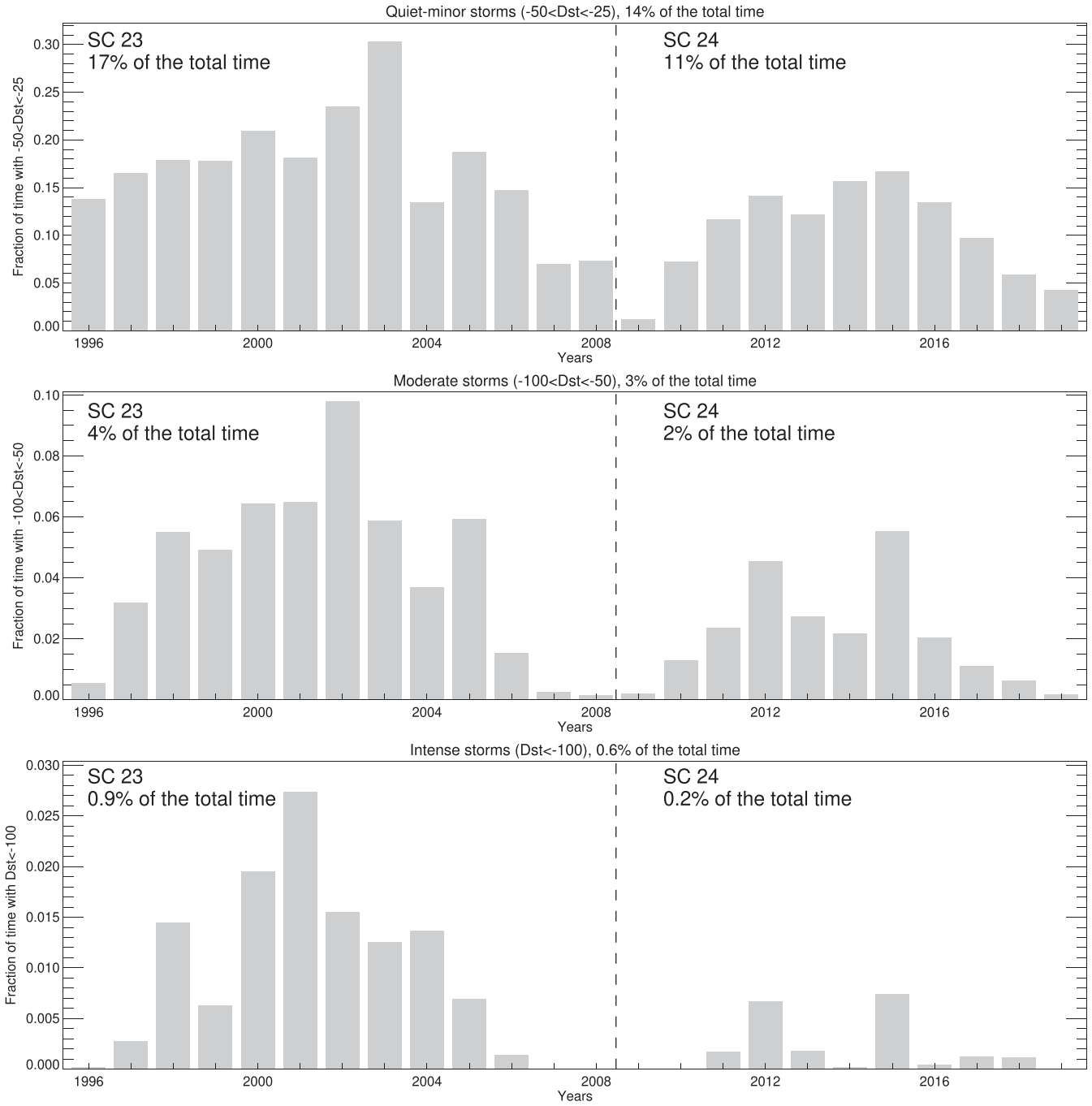

Figure 16. The temporal evolutions of the fractions of time (in the total considered period of time) when quite minor (upper panel), moderate (middle panel), and intensive (bottom panel) storms were observed.

that the YTXPF of solar flares is most correlated with storms of different intensities. It exhibits higher correlation coefficients than the SSN. The YTMLRs are moderately correlated with the YMDIs. But the correlation coefficients are much larger than those for the YORC. We observe a very significant correlation ($cm^3 = 0.82$) between the YTMLR of the most massive events with moderate storms. It is also noteworthy that the YTMLR of the most massive CMEs is only moderately correlated ($cm^3 = 0.62$) with the most intensive storms. This means that the mass of the CMEs is not a very significant factor in determining the geoeffectiness of CMEs. Analyzing the values of the correlation coefficient, we must remember that the geoefficiency of CMEs depends mostly on two factors: their velocity and the Bz component (perpendicular to the ecliptic plane) of the magnetic field contained in the interplanetary CMEs (Gopalswamy 2010b). The magnetic field carried by the CMEs is not correlated with any of the parameters of solar activity analyzed in this study. Therefore, it does not affect our analysis. The second factor, the speed of the CMEs, is very well represented by the YTXPF. The YTXPF, reflecting the maximum X-ray fluxes for flares, is a measure of the initial CME acceleration (Nicewicz & Michalek 2016). Therefore, the YTXPF is best correlated with the YMDI. On the other hand, the YORC, which in the

Table 4
Correlation Coefficients for the Parameters Considered in This Study (SSN, YORC, YTMLR, and YTXPF) and the Yearly Mean Dst Index Displayed in Figure 15

	SSN[a]	YORC[b]	YTMLR[c] of the least massive	YTMLR of the medium massive	YTMLR of the most massive	YTMLR of all CMEs	YTXPF[d]
Quite minor/weak geomagnetic storms, $-25\text{nt} \leqslant \text{Dst} < -50\text{nT}$							
Fraction of time	0.69	0.21	0.48	0.55	0.70	0.65	0.78
Moderate geomagnetic storms, $-100\text{nT} < \text{Dst} \leqslant -50\text{nT}$							
Fraction of time	0.82	0.33	0.55	0.71	0.82	0.79	0.82
Intense geomagnetic storms, $\text{Dst} \leqslant -100$ nT							
Fraction of time	0.78	0.15	0.41	0.62	0.62	0.63	0.83

Notes.
[a] Sunspot number.
[b] Yearly occurrence rate of CMEs.
[c] Yearly total mass-loss rate.
[d] Yearly total X-ray peak flux of flare.
[e] Yearly mean Dst index.

period of minimum solar activity between SC 23 and SC 24 is dominated by a large population of low-energy events, correlates poorly with the YMDI.

4. Conclusions

In this study, we evaluated the temporal evolution of the total mass ejected from the Sun through CMEs in SCs 23 and 24. Since the determination of mass is subject to considerable uncertainty, we have carried out an extensive statistical analysis based on the total mass ejected in each year. The main results of this study are summarized below.

1. The YTMLR tracks the SSN much better than the CME detection rate. The correlation coefficient between the SSN and YTMLR is 0.86, but still this correlation is not perfect (Figure 3). Although in SC 24 we observe a decrease in the YTMLR compared to SC 23, this decrease is not as significant as in the case of the SSN. We estimate that in SC 24 the Sun should eject up to 90% of the total mass ejected in SC 23. Therefore, we conclude that the TMLR from the Sun through CMEs does not depend significantly on the strength of the cycle and the CME occurrence rate. This mass, however, is carried by different sets of events in different cycles. The average mass of all ejections is 1.55e+15g, but it was up to 1.79e+15g in SC 23 and only 1.34e+15g in SC 24 (30% less compared to SC 23).
2. The mass carried out by numerous CMEs without known mass (35% of all of the recorded CMEs) can only contribute up to 9% of the total mass ejected from the Sun through CMEs. This means that the CME mass included in the CDAW catalog reflects the actual MLR from the Sun.
3. The high-mass events (mass > 7.0e+15g) eject mass from the Sun more significantly in the final phase of maximum solar activity. This increased rate of mass loss must be associated with eruptions of PCFs. For this reason, the YTMLR through the high-mass events is the least correlated with the SSN in comparison to the other samples of CMEs (the correlation coefficient is 0.75). On the other hand, the YTMLR though the intermediate-mass and low-mass events tracks the SSN almost perfectly (the correlation coefficient is 0.89). This means that such events are associated with active regions.
4. It was demonstrated the most pronounced contributions to the TML are due to CMEs having angular widths in the range from 50° to 120° (60% of the TML) and halo events. The very important result is that the halo events, which make up only 2.5% of all of the recorded CMEs, carry about 20% of the total mass ejected from the Sun (similar in both solar cycles). The remaining mass is lifted out by partial halo events (about 20% of the total ejected mass).
5. The CME mass distribution in the log-lin representation reflects the Gaussian distribution very well. We can state that the CMEs included in the CDAW catalog form one coherent population of ejections and identifications. This is in line with the theory presented by Aoki et al. (2004). They suggested that the physical quantities associated with mass outflows should demonstrate log-normal distributions.
6. The YTMLR is very well correlated to the other solar activity indicators considered (SSN, YOROC, YTMLR, and YTXPF; the cm^3 is more than 0.78 for all of them). The YTMLR seems to be the most universal indicator of solar activity.
7. Unlike the YORC, the YTMLR is correlated with the Dst index. The most significant correlation observed is for the YTMLR for the most massive events and moderate geomagnetic storms ($cm^3 = 0.82$). The striking feature is that the YTMLR for the most massive events is only moderately correlated with the most intensive geomagnetic storms ($cm^3 = 0.62$).
8. It turns out that the YTXPF of solar flares is a very good indicator of solar (SSN) and space (Dst) activity. We would like to thank the reviewer for substantive comments and constructive cooperation during the correction of the article.

This work was supported by NASA's LWS program.

ORCID iDs

Grzegorz Michalek https://orcid.org/0000-0001-6848-971X
Nat Gopalswamy https://orcid.org/0000-0001-5894-9954
Seiji Yashiro https://orcid.org/0000-0002-6965-3785

References

Abramenko, V. I., & Longcope, D. W. 2005, ApJ, 619, 1160
Aoki, S. I., Yashiro, S., & Shibata, K. 2004, arXiv:astro-ph/0401352
Boursier, Y., Lamy, P., Llebaria, A., Goudail, F., & Robelus, S. 2009, SoPh, 257, 125
Brueckner, G. E., Howard, R. A., Koomen, M. J., et al. 1995, SoPh, 162, 357
Byrne, J. P., Morgan, H., Habbal, S. R., & Gallagher, P. T. 2012, ApJ, 752, 145
Carbonell, M., Terradas, J., Oliver, R., & Ballester, J. L. 2007, A&A, 476, 951
Chowdhury, P., Choudhary, D. P., & Gosain, S. 2013, ApJ, 768, 188
Chowdhury, P., Kilcik, A., Yurchyshyn, V., Obridko, V. N., & Rozelot, J. P. 2019, SoPh, 294, 142
Colaninno, R. C., & Vourlidas, A. 2009, in Solar Heliospheric and INterplanetary Environment (SHINE 2009), 166
Deng, L., Zhang, X., An, J., & Cai, Y. 2017, JSWSC, 7, A34
Domingo, V., Fleck, B., & Poland, A. I. 1995, SoPh, 162, 1
Dumbović, M., Čalogović, J., Vršnak, B., et al. 2018, ApJ, 854, 180
Gopalswamy, N. 2009, in Climate and Weather of the Sun-Earth System (CAWSES): Selected Papers from the 2007 Kyoto Symposium, ed. T. Tsuda et al. (Tokyo: Terrapub), 77
Gopalswamy, N. 2010b, in IAU Symp. 264, Solar and Stellar Variability: Impact on Earth and Planets, ed. A. G. Kosovichev, A. H. Andrei, & J.-P. Rozelot, Vol. 264 (Cambridge: Cambridge Univ. Press), 326
Gopalswamy, N. 2016, GSL, 3, 8
Gopalswamy, N. 2018b, in IAU Symp. 340, Long-term Datasets for the Understanding of Solar and Stellar Magnetic Cycles (Cambridge: Cambridge Univ. Press), 95
Gopalswamy, N., Aguilar-Rodriguez, E., Yashiro, S., et al. 2005b, JGRA, 110, A01207
Gopalswamy, N., Akiyama, S., Yashiro, S., et al. 2014, GeoRL, 41, 2673
Gopalswamy, N., Akiyama, S., Yashiro, S., et al. 2020, JPhCS, 1620, 012005
Gopalswamy, N., Akiyama, S., Yashiro, S., & Mäkelä, P. 2010, ASSP, 19, 289
Gopalswamy, N., Alejandro, L., Yashiro, S., Nunes, S., & Howard, R. 2003b, in Int. Solar Cycle Studies (ISCS) Symp., Solar Variability as an input to the Earth's Environment, ed. A. Wilson (Noordwijk: ESA Publications Division)
Gopalswamy, N., Lara, A., Yashiro, S., & Howard, R. A. 2003a, ApJL, 598, L63
Gopalswamy, N., Mäkelä, P., Yashiro, S., & Akiyama, S. 2018, JASTP, 176, 26
Gopalswamy, N., Nunes, S., Yashiro, S., & Howard, R. 2004, AdSpR, 34, 391
Gopalswamy, N., Xie, H., Akiyama, S., et al. 2015a, ApJL, 804, L23
Gopalswamy, N., Xie, H., Yashiro, S., et al. 2012, SSRv, 171, 23
Gopalswamy, N., Yashiro, S., & Akiyama, S. 2006, in Proc. ILWS Workshop, ed. N. Gopalswamy & A. Bhattacharyya, 79
Gopalswamy, N., Yashiro, S., & Akiyama, S. 2015b, ApJ, 809, 106
Gopalswamy, N., Yashiro, S., & Akiyama, S. 2016, ApJL, 823, L15
Gopalswamy, N., Yashiro, S., Liu, Y., et al. 2005a, JGRA, 110, A09S15
Gopalswamy, N., Yashiro, S., Michalek, G., et al. 2009, Earth, Moon, and Planets, 104, 295
Gopalswamy, N. 2010a, in 20th National Solar Physics Meeting, ed. I. Dorotovic, 108
Gopalswamy, N. 2018a, in Extreme Events in Geospace, ed. N. Buzulukova (Amsterdam: Elsevier), 37
Hess, P., & Colaninno, R. C. 2017, ApJ, 836, 134
Howard, R., Brueckner, G., St., Cyr, O., et al. 2013, GMS, 99, 17
Howard, R. A., Moses, J. D., Vourlidas, A., et al. 2008, SSRv, 136, 67
Kahler, S. W. 1992, ARA&A, 30, 113
Kaiser, M. L., Kucera, T. A., Davila, J. M., et al. 2008, SSRv, 136, 5
Lamy, P. L., Floyd, O., Boclet, B., et al. 2019, SSRv, 215, 39
Lara, A., Gopalswamy, N., Niembro, T., Pérez-Enríquez, R., & Yashiro, S. 2020, A&A, 635, A112
Loewe, C. A., & Prölss, G. W. 1997, JGR, 102, 14209
MacQueen, R. M., Csoeke-Poeckh, A., Hildner, E., et al. 1980, SoPh, 65, 91
MacQueen, R. M., Eddy, J. A., Gosling, J. T., et al. 1974, ApJ, 187, L85
Manchester, W., Kilpua, E. K. J., Liu, Y. D., et al. 2017, SSRv, 212, 1159
Michalek, G., Gopalswamy, N., & Yashiro, S. 2019, ApJ, 880, 51
Michels, D. J., Howard, R. A., Koomen, M. J., & Sheeley, N. R. Jr. 1980, in IAU Symp. 86, Radio Physics of the Sun, ed. M. R. Kundo & T. E. Gergely (Dordrecht: Reidel), 439
Mishra, W., Srivastava, N., Wang, Y., et al. 2019, MNRAS, 486, 4671
Moss, D., Saar, S. H., & Sokoloff, D. 2008, MNRAS, 388, 416
Munro, R. H., Gosling, J. T., Hildner, E., et al. 1979, SoPh, 61, 201
Nicewicz, J., & Michalek, G. 2016, SoPh, 291, 1417
Olmedo, O., Zhang, J., Wechsler, H., Poland, A., & Borne, K. 2008, SoPh, 248, 485
Petrie, G. J. D. 2015, ApJ, 812, 74
Poland, A. I., Howard, R. A., Koomen, M. J., Michels, D. J., & Sheeley, N. R. J. 1981, SoPh, 69, 169
Robbrecht, E., & Berghmans, D. 2004, A&A, 425, 1097
Selvakumaran, R., Veenadhari, B., Akiyama, S., et al. 2016, JGRA, 121, 8188
Sokoloff, D., & Nesme-Ribes, E. 1994, A&A, 288, 293
St. Cyr, O. C., Howard, R. A., Sheeley, N. R., et al. 2000, JGRA, 105, 18169
Takahashi, S., Iyemori, T., & Takeda, M. 1990, JGG, 42, 1325
Tousey, R. 1973, in Space Research XIII, Vol. 2 (Berlin: Akademie-Verlag), 713
Verbanac, G., Živković, S., Vršnak, B., Bandić, M., & Hojsak, T. 2013, A&A, 558, A85
Vourlidas, A., Balmaceda, L. A., Stenborg, G., & Lago, A. D. 2017, ApJ, 838, 141
Vourlidas, A., Howard, R. A., Esfandiari, E., et al. 2010, ApJ, 722, 1522
Vourlidas, A., Lynch, B. J., Howard, R. A., & Li, Y. 2013, SoPh, 284, 179
Vourlidas, A., Subramanian, P., Dere, K. P., & Howard, R. A. 2000, ApJ, 534, 456
Vourlidas, A., & Webb, D. F. 2018, ApJ, 861, 103
Vršnak, B., Ruždjak, D., Sudar, D., & Gopalswamy, N. 2004, A&A, 423, 717
Webb, D. F., Gibson, S. E., Hewins, I. M., et al. 2018, FrASS, 5, 23
Webb, D. F., & Howard, T. A. 2012, LRSP, 9, 3
Webb, D. F., Howard, R. A., St., Cyr, O. C., & Vourlidas, A. 2017, ApJ, 851, 142
Yashiro, S., Gopalswamy, N., Akiyama, S., & Howard, R. A. 2006, in 36th COSPAR Scientific Assembly, 1778
Yashiro, S., Gopalswamy, N., Michalek, G., et al. 2004, JGR, 109, A07105
Yashiro, S., Michalek, G., & Gopalswamy, N. 2008, AnGeo, 26, 3103
Zolotova, N. V., & Ponyavin, D. I. 2006, A&A, 449, L1